Structural evolution of a Ni/NiO$_x$ based supercapacitor in cyclic charging-discharging: A polarized neutron and X-ray reflectometry study

Zhe Li [a, 1], Xinzhi Liu [b, 1, 2], Grace L. Causer [b, c], Ko-Wei Lin [b, d], Philip Pong [e], Stephen A. Holt [b], Frank Klose [b, f, **], Yang Yang Li [a, *]

[a] Department of Materials Science and Engineering, City University of Hong Kong, 83 Tat Chee Ave, Hong Kong
[b] Australian Nuclear Science and Technology Organisation, New Illawarra Rd, Lucas Heights, NSW 2232, Australia
[c] Institute for Superconducting and Electronic Materials, University of Wollongong, Northfield Ave, Wollongong, NSW 2500, Australia
[d] Department of Materials Science and Engineering, National Chung Hsing University, Taichung 402, Taiwan
[e] Department of Electrical and Electronic Engineering, The University of Hong Kong, Pokfulam Rd, Hong Kong
[f] Material Science and Engineering Program, Guangdong Technion - Israel Institute of Technology, Shantou 515063, China

ARTICLE INFO

ABSTRACT

Ni/Ni-oxide based supercapacitors with their excellent stability and long cycle lifetime are favorable due to their cost effectiveness and practicality. And yet, the full picture of their cyclic charging-discharging process is not well understood, and the influential factors on the cycle life of a supercapacitor are complicated. Using a combined polarized neutron and X-ray reflectometry approach, we have studied the structural evolution of a layered Ni/NiO$_x$ supercapacitor electrode, operated in an alkaline electrolyte for cyclic charging-discharging. For the lower thousands of cycles, oxidation of Ni current-collecting backbone and dissolution of outer Ni oxide electroactive materials contribute to a total thickness consumption of 2 nm. Upon higher thousands of cycles, the two-dimensional NiO$_x$ surface-layer evolves into a three-dimensional porous network as a result of the "hole drilling" depletion behavior of Ni oxide, i.e., dissolution of the "more porous" part and preservation of the "more compact" part in the NiO$_x$ layer. The extra surface area of the Ni/NiO$_x$ supercapacitor generated after cyclic charging-discharging gives rise to an increased capacitance. Evidenced by the increased derived density, the crystal defects of inner-layer NiO$_x$ are also eliminated with cycling, probably through Ni atom rearrangement, filling of oxygen vacancies within NiO$_x$, or both.

© 2018 Elsevier Ltd. All rights reserved.

1. Introduction

Ni and Ni oxide composite materials, possessing the merits of earth-abundance, low cost, and easy processing, have been widely studied in diverse fields, such as bio-medicine [1], bio-sensing [2], electronics [3], energy storage [4,5], magnetics [6], and optics [7]. Ni/NiO nanocomposites in the structures of zero to three

dimensions have been reported and the fabrication strategies are generally divided into two categories: (a) self-conversion: building up a nanostructured Ni followed by oxidation treatment to the surface, or conversely, partially reducing a nanostructured Ni oxide in a reductive environment; (b) external introduction: deposition of nanostructured Ni oxides on Ni metal substrates (e.g., Ni foams). Particularly in energy storage, Ni/NiO nanocomposites not only exhibit excellent capacity, cycling stability, and rate capability as anodes of lithium-ion batteries [5,8], but also offer superior specific capacitance, cycling stability, power and energy densities as supercapacitor electrodes [4,9]. Supercapacitors bridge the gap between conventional capacitors and rechargeable batteries. They simultaneously exhibit rapid charging-discharging and battery-like high electrical capacitance. Typically, for a Ni/NiO supercapacitor electrode operated in an alkaline electrolyte, fast and reversible

* Corresponding author.
** Corresponding author. Material Science and Engineering Program, Guangdong Technion - Israel Institute of Technology, Shantou 515063, China.
   E-mail addresses: frank.klose@gtiit.edu.cn (F. Klose), yangli@cityu.edu.hk (Y.Y. Li).
   [1] These authors contributed equally to this work.
   [2] Current address: Helmholtz-Zentrum Berlin fur Materialien und Energie, Hahn-Meitner-Platz 1, 14109, Berlin, Germany.

redox reactions occur via the equation: $Ni^{II}O + OH^- \leftrightarrow Ni^{III}OOH + e^-$. That is, in the charging state, OH^- anions are absorbed and intercalated in the crystal lattice of surface NiO to temporarily form a thin layer of NiOOH and charge (electrical energy) is stored. While in the discharging state, NiOOH is reduced to NiO with deintercalation of OH^- anions and the charge (electrical energy) is released [10]. A majority of reported Ni/NiO supercapacitor electrodes undergo capacitance decay after large numbers of charging-discharging cycles. It is explained by that, on one hand, repeated intercalation-deintercalation of OH^- anions leads to a breaking of the NiO crystal structure, and on the other hand, the Ni backbone may be gradually oxidized and this results in a weakened mass transport [11,12]. However, as observed in some recent publications, capacitances of Ni/NiO supercapacitors increase with continuous charging-discharging up to thousands of cycles [9,13–17]. Therefore, influential factors for the cycle life of a supercapacitor electrode are complicated. The full picture of the cyclic charging-discharging process, including electrolyte-electrode interaction and electrode structure variation, is yet to be comprehended by experiment [9,18].

Neutron reflectometry (NR), often combined with X-ray reflectometry (XRR), is a mature technique for studying thin films and multi-layer interfaces, such as in inorganic magnetic materials [19], polymers [20], and bio-membranes [21]. The method takes advantage of the neutrons' strong material penetration capability, sub-angstrom resolution in thickness, and high light-element sensitivity. NR measures the reflectivity of a neutron beam at small scattering angles as a function of the scattering vector Q. For a specular reflected neutron beam, Q is directed perpendicular to the sample surface, and its magnitude is expressed as follows: $Q = 4\pi\sin\theta/\lambda$, where θ is the reflection angle and λ is the wavelength of the incident neutron beam. An analysis of a polarized neutron reflectometry (PNR) experiment will reveal the chemical and magnetic depth-profile of a thin film along the surface normal direction, (i.e., in the direction of Q), by determining the depth-dependence of the local in-plane averaged scattering length density (SLD), the latter being a measure of the material's scattering ability [22–24]. The nuclear SLD of a given volume-element is the product of the bound coherent scattering length b_{nuc} of a given isotope and the atomic density N of that isotope within the volume-element. If the material is made up of several elemental isotopes, the total SLD is the sum of the individual isotopic SLDs. In addition, if the volume-element carries a net magnetic moment, then a magnetic SLD will also result, which is proportional to the magnetic scattering length $\pm b_{mag}$. The "$\pm$" symbol applies when the polarization direction of the incident neutron beam is oriented parallel (spin up (R+)) or antiparallel (spin down (R-)) to the magnetizing sample field. The total local neutron SLD is, therefore, given by: $SLD_{total} = SLD_{total\ nuc} \pm SLD_{total\ mag} = (b_{nuc\ 1} \pm b_{mag\ 1}) \times N_1 + (b_{nuc\ 2} \pm b_{mag\ 2}) \times N_2 \dots$ [25,26]. X-ray reflectometry (XRR) is conceptually very similar to NR, however, because X-rays interact with the electron clouds of atoms, X-ray SLDs scale with the local electron density as $b_{X-ray} = r_e \times f_1$, where r_e is the classical electron radius and f_1 is the real part of the atomic scattering factor [27,28]. As a result, XRR is particularly powerful for investigating interfaces between light and heavy materials, but lacks sensitivity to detect interfacial details between layers which have similar electron concentrations. In contrast to NR, magnetic scattering is very weak in XRR and can usually be omitted [27–29]. In electrochemistry, NR has been utilized not only for fundamental research into transition metal oxides [30] and conducting polymers [31], but also into lithium-ion batteries, particularly in aspects of solid electrolyte interphase formation [32,33], lithiation of amorphous silicon electrodes [34,35], and lithium permeation through Si [36,37]. Studies of supercapacitors using NR or XRR are limited, despite the

great potential to undertake *in situ* monitoring of layer changes of electrode materials, and to reveal details of electrochemical reactions at interfaces [38].

In the present study, we simplify the Ni/NiO supercapacitor electrode into a layered Ni/NiO$_x$ model, and study its cyclic charging-discharging properties in a deuteroxide (D$_2$O)-based sodium hydroxide (NaOH) solution electrolyte, via the combination of *in situ* PNR and *ex situ* XRR techniques. Owing to the great penetration capability of neutron beams (here through the Si substrate), PNR measurements can be performed *in situ*, which is not possible using a comparable X-ray based reflectometry experimental setup. The electrolyte-electrode interaction and associated structural and compositional changes at the electrode, can therefore be monitored directly, while unnecessary adverse effects resulting from sample cleaning procedures, electrolytic cell assembly, etc. are eliminated. For the particular case of Ni/NiO, it is difficult to pinpoint possible charging-discharging induced layer and interface changes by XRR or standard unpolarized NR, because bulk Ni and NiO have very similar structural SLD values for both X-rays and neutrons (Ni: $9.414 \times 10^{-6}\,\text{Å}^{-2}$ for NR and $6.44 \times 10^{-5}\,\text{Å}^{-2}$ for XRR; NiO: $8.66 \times 10^{-6}\,\text{Å}^{-2}$ for NR and $4.82 \times 10^{-5}\,\text{Å}^{-2}$ for XRR). Therefore, PNR is applied in our study. Since Ni is ferromagnetic (bulk: 0.60 μ_B per Ni atom at 298 K resulting in a total SLD of $10.87 \times 10^{-6}\,\text{Å}^{-2}$ for spin up neutrons and $7.94 \times 10^{-6}\,\text{Å}^{-2}$ for spin down neutrons), and NiO is antiferromagnetic (nil net magnetic moment resulting in nil magnetic SLD), distinctly different PNR patterns can be expected for spin-up (R^+) and spin-down (R^-) polarized neutron beams. The ferromagnetism of the Ni layer induces neutron spin up/down scattering contrast to identify not only the density of the Ni layer, but also its net magnetization. Consistent refinement of PNR and XRR data allows to identify the density and composition profiles of the layered system with higher precision. This allows, for the case of PNR, the extraction of both chemical (nuclear) SLD and magnetic SLD profiles as a function of sample depth, and, using the same set of structural parameters in the analysis of the XRR data, the chemical (electronic) SLD depth profile is extracted. As such, during the charging-discharging process, the degradation of the Ni/NiO$_x$ electrode is measured; moreover, the structural and compositional variations within the NiO$_x$ layer are monitored.

2. Experimental details

2.1. Sample fabrication and morphology characterization

A dual ion-beam sputtering deposition system was employed to grow a NiO$_x$ layer on top of a Ni layer, on a p-type low-resistivity naturally-oxidized Si wafer substrate [39]. A Kaufman source was used to focus an Ar$^+$ beam onto the Ni sputtering target (Commonwealth Scientific Corp.); while an End-Hall source was used to either clean the Si substrate (prior to deposition) or *in situ* bombard the sample during NiO layer deposition. The voltage of the End-Hall source was fixed at 70 V throughout the deposition to ensure a constant ion energy with an estimated flux of 2.1×10^{18} Ar$^+$ cm^{-2} s^{-1}. The O$_2^+$/Ar$^+$ ratio in the End-Hall source was fixed to 15%. No external magnetic fields were applied during the deposition process.

The original and eventual morphologies of the as-prepared Ni/NiO$_x$ sample were examined with a transmission electron microscope (TEM, JEOL-2100F), and a scanning electron microscope (SEM, Philips XL 30FEG), respectively. The high-angle XRD patterns were collected using an X-ray diffractometer (Bruker, D2phaser) with a radiation source of Cu Kα ($\lambda = 0.15406$ nm). The scan range was between $30°$ and $70°$ at a scan rate of $0.2°$ s^{-1}.

2.2. Cyclic charging-discharging test

A sealed three-electrode system controlled by a potentiostat (Autolab, PG302N) was employed for the cyclic voltammetry (CV) charging-discharging measurements (Fig. 1 a). The Ni/NiO$_x$ sample was assigned as the working electrode, a Au sputtered low-resistivity p-type Si wafer as the counter electrode, a saturated calomel electrode (SCE) as the reference electrode, and a 1 M D$_2$O-based NaOH solution was the electrolyte. CV charging-discharging measurements were carried out in the potential range from 0 to 0.65 V at a scan rate of 0.1 V s^{-1}, and tested for up to 20,000 cycles.

2.3. PNR, XRR measurement, and data analysis

PNR measurements were *in situ* conducted on the PLATYPUS neutron reflectometer located at the Australian Nuclear Science and Technology Organization (ANSTO) [40,41]. All PNR measurements were recorded at room temperature, directly after the cyclic charging-discharging of the Ni/NiO$_x$ sample. Prior to measurement the sample was magnetically saturated in a *ca.* 1000 Oe field. During measurement, a 20 Oe guide field was used to keep the Ni layer magnetically saturated and to prevent depolarization of the spin-polarized neutron beam traversing the sample region. The neutron beam entered the Si substrate of the Ni/NiO$_x$ sample, and was partially reflected, successively by the Ni layer, NiO$_x$ layer, and NaOH/D$_2$O electrolyte surfaces (Fig. 1 a). XRR measurements were *ex situ* conducted on an X-ray reflectometer (Rigaku, D/MAX2500V2) equipped with a Cu K$_\alpha$ source ($\lambda = 0.15406$ nm). The Ni/NiO$_x$ sample was taken out of the electrolyte, cleaned with distilled water, and dried under N$_2$ gas, before measurement. The X-ray beam entered the NiO$_x$ surface-layer of the sample, and was partially reflected, successively by the NiO$_x$ layer, Ni layer and Si substrate surfaces (Fig. 1 b). The fitting and analyses of PNR and XRR data were carried out with the SimulReflec software [42]. Since the PNR and XRR experiments could not be conducted simultaneously in the same experimental set-up using the exact same sample piece, two different sample pieces (produced in the same film manufacturing run) were used in individual set-ups.

3. Results and discussion

The as-prepared Ni/NiO$_x$ sample consists of crystalline Ni and NiO, confirmed by the XRD patterns (Fig. 2 a). Despite a nominal bilayer of Ni/NiO being deposited, the NiO layer usually consists of a mixture of NiO and unoxidized Ni, resulting in an actual layer of NiO$_x$ [43]. Additionally, sputter-deposited thin films, particularly when not deposited at elevated temperatures, generally possesses an actual density lower than its bulk counterparts, and samples of nanocrystalline and intrinsic porosity are to be expected. (Note the "intrinsic pores" are merely closed pores generated by imperfect Ni atom arrangement and do not allow electrolyte penetration.) By cross-sectional TEM image (Fig. 2 b), the Ni and NiO$_x$ layers are approximately 75 and 25 nm in thickness, respectively, and a distinct interface between Ni and NiO$_x$ is visible.

CV curves of the Ni/NiO$_x$ sample after completion of up to 20,000 cycles of charging-discharging are plotted (Fig. 3). Since the
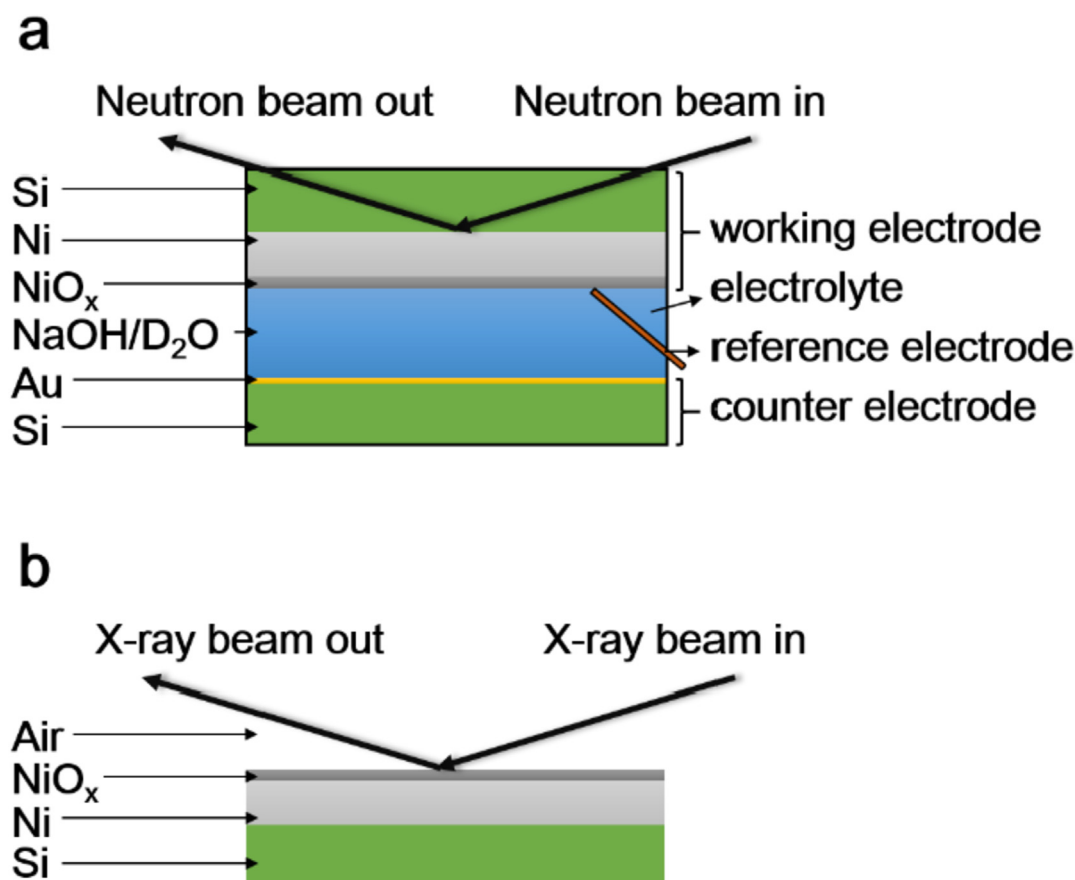

Fig. 1. Schematic diagrams of the Ni/NiO$_x$ sample layout and beam paths for the (a) CV cyclic charging-discharging with *in situ* PNR measurements and (b) *ex situ* XRR measurements.
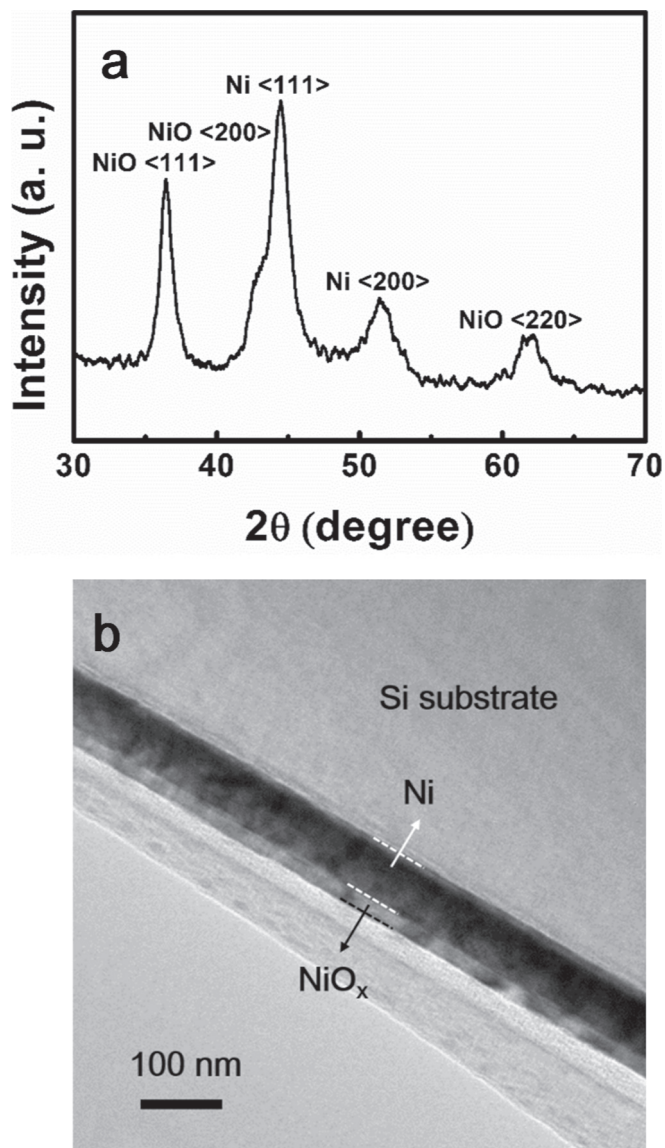
Fig. 2. As-prepared Ni/NiO$_x$ sample: (a) XRD patterns and (b) cross-sectional TEM image.

number of OH$^-$ anions from the NaOH are negligible compared to that of OD$^-$ anions from the D$_2$O electrolyte, Ni deutroxides (i.e. Ni^{II}(OD)$_2$ and Ni^{III}OOD) are considered to form as the reaction products in the electrochemical redox reactions. For the lower thousands of cycles, the oxidation-peak, indicating the charge storage process, is observed at *ca.* 0.5 V, where Ni^{III}OOD forms through electrochemical oxidation of Ni^{II}O. While the reduction-peak, indicating the charge release process, is observed at *ca.* 0.3 V, where Ni^{III}OOD is converted to Ni^{II}O through electrochemical reduction. As the cycle number reaches 20,000, the oxidation-peak gradually shifts to higher voltage (*ca.* 0.55 V), while the reduction-peak gradually shifts to lower voltage (*ca.* 0.15 V). Meanwhile, the current of the oxidation-peak rises from 5 mA to 14 mA, and the reduction-peak increases from −5 mA to −12 mA. Note that at lower thousands of cycles, the CV curves display symmetrical redox peak shapes and heights (current intensity), which, however, become asymmetric at higher cycle numbers. This reflects that the irreversible redox reactions occurring on the Ni/NiO$_x$ electrode are more prominent at higher thousands of cycles, which is related to

structural changes, compositional changes, or both. The shape of the oxidation peak abruptly changes from a rounded peak shape (below 6000 cycles) to a sharp peak shape (above 9000 cycles). The peak shape (width) is related to the number of electrons involved in the reaction at each stage of the cycling process. In the case of Ni/NiO$_x$, oxidation of Ni to Ni^{II}O and Ni^{II}O to Ni^{III}OOH co-exist in the regime up to 6000 cycles with multiple electrons involved in the reaction, leading to broad and rounded oxidation peaks. Above 9000 cycles the oxidation of Ni^{II}O to Ni^{III}OOH dominates which involves only a single electron, leading to sharper oxidation peak shapes. The capacitances (C, mF) of the Ni/NiO$_x$ sample are calculated by integrating CV curves via equation: = d 000, 6000, 10000 and 20000 cycles $C = (\int I\,\Delta v)/(2\Delta VS)$ n where ΔV is the potential window of 0.65 V, and S is the scan rate of 0.1 V s^{-1}. The capacitance of the Ni/NiO$_x$ electrode increases from 14.7 mF (1000 cycles), 15.2 mF (3000 cycles), 16.8 mF (6000 cycles), 17.4 mF (9000 cycles), 17.8 mF (10,000 cycles), 20.1 mF (13,000 cycles), 22.5 mF (16,000 cycles), 22.7 mF (19,000 cycles) up to 24.4 mF (20,000 cycles).

The experimental and fitting results of *in situ* PNR, before and after cycling the Ni/NiO$_x$ sample through 3000 charging-discharging cycles, are shown in Fig. 4(a). In the PNR patterns, the clear splitting of the spin-up (R$^+$) and spin-down (R$^-$) polarized beam reflectivities indicates a strong Ni magnetization. The periodic oscillation in the reflectivity intensity, observed in the Q range from 0.2 to 0.4 nm^{-1} results from the total Ni + NiO$_x$ layer thickness, which can be estimated by $2\pi/\Delta Q$, where ΔQ is the width of a single period in Q space. The experimental spin asymmetry (ASY) data and corresponding fits are shown in Fig. 4(b), which result solely from a magnetic effect. The quality of the modeled magnetic depth profile can be evaluated in detail, as it has to fit the measured ASY data: ASY = (R$^+$ - R$^-$)/(R$^+$ + R$^-$) as a function of the scattering vector Q. As can be seen from Fig. 4(a), the difference between before cycling and after 3000 cycles is quite small. However, according to analysis, two variations can be credibly determined: (1) the overall thickness of Ni + NiO$_x$ is slightly reduced (*ca.* 2 nm) and (2) the SLD contrast around the Ni/NiO$_x$ interface is prominently reduced. Note the prominent change in reflectivity after 3000 cycles appearing around 0.5−0.6 nm^{-1}, especially in the ASY curves (red box in Fig. 4 b). The latter is related to the modified magnetic contrast between the Ni and NiO$_x$ near the interface with increased cycling.

Due to the limited available beam time for PNR measurement, the structural and compositional changes of the Ni/NiO$_x$ sample upon larger numbers of cycles are investigated by *ex situ* XRR. The experimental and fitted reflectivities as a function of Q before cycling, and after 3,000, 6,000, 10,000 and 20,000 cycles of charging-discharging are plotted (Fig. 5). The very pronounced layer thickness oscillations, visible between the total reflectivity edge and Q = 2 nm^{-1}, result from a periodicity of about 25 nm that corresponds to the NiO$_x$ layer. There is also a long wavenumber oscillation, with a first maximum located midway between the critical edge and the minimum at about Q = 4.5 nm^{-1}, and a second maximum at about Q = 5.5 nm^{-1}. This oscillation is attributed to a 2 nm layer at the outer surface of the NiO$_x$ layer, which was also found when analyzing the PNR data. The zoom-in of the 10,000 cycles at low Q range (Fig. 5 inset) reveals that a characteristic high-frequency oscillation periodicity is superimposed on the major oscillation patterns after 10,000 cycles, which is related to the total thickness of the Ni + NiO$_x$ bilayer (*ca.* 104 nm). The amplitude of the thickness oscillations becomes more and more damped with increasing cycle numbers. This is due to a reduced interfacial scattering contrast in real space, i.e., a more pronounced roughness of the interface profiles with increasing cycle numbers. The fitting of the Q-dependent primary intensity oscillation features of PNR
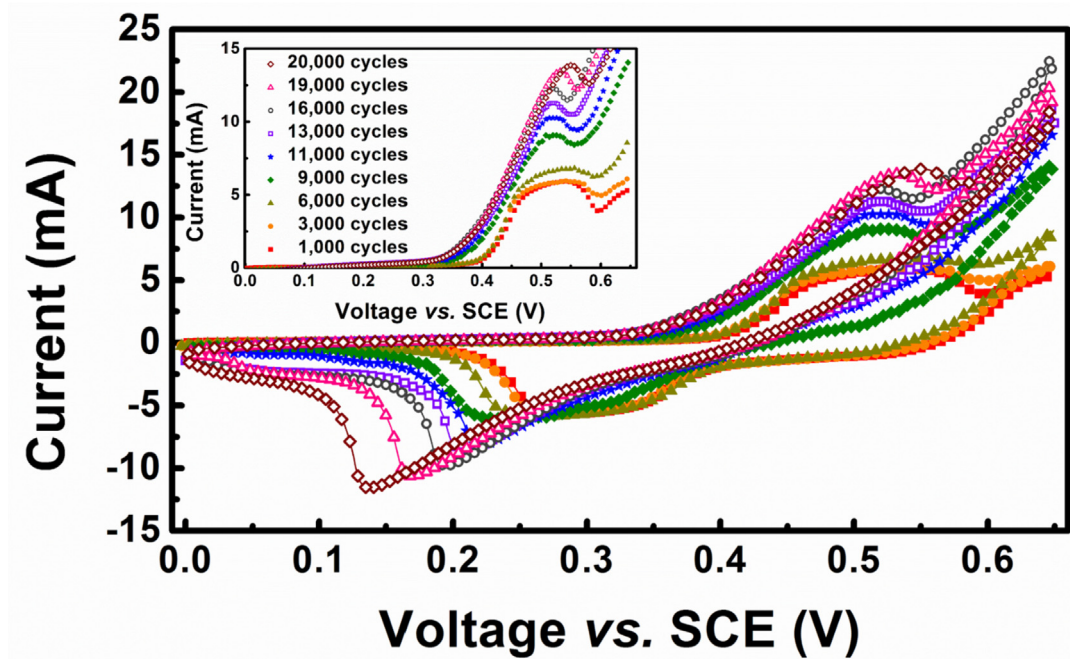
Fig. 3. CV curves of the Ni/NiO$_x$ sample after charging-discharging in a 1 M NaOH D$_2$O solution for up to 20,000 cycles at a scan rate of 0.1 V s^{-1}. Inset: magnified oxidation-peak profiles in the positive scan.
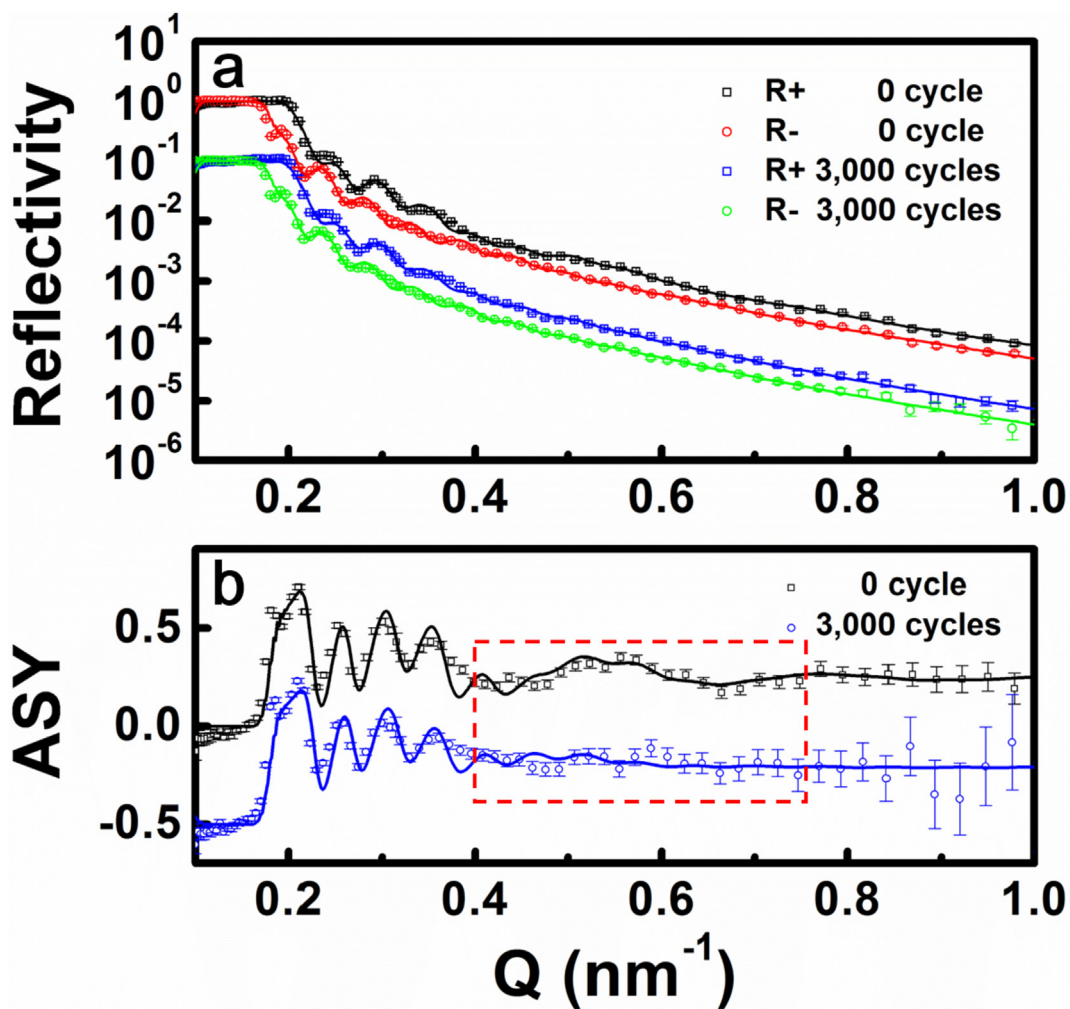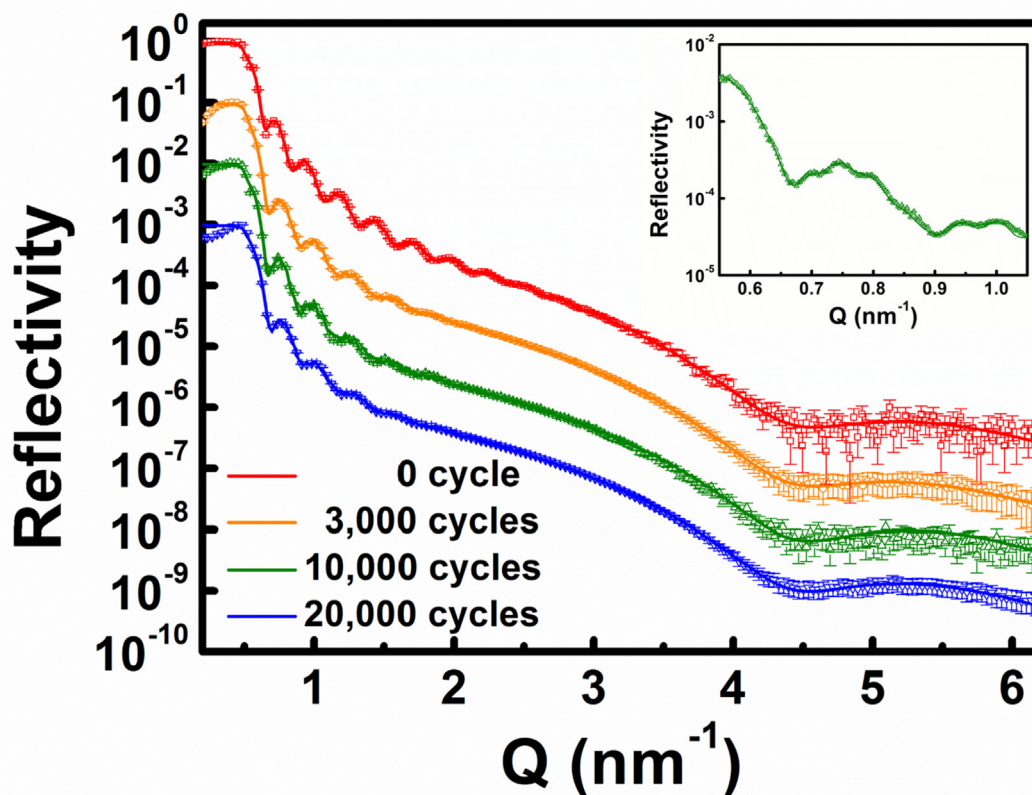

Fig. 4. PNR measurement before cycling and after 3000 charging-discharging cycles, with experimental data (symbols) and fits (lines): (a) spin-up (R+) and spin down (R-) reflectivity as a function of Q; (b) spin ASY as a function of Q. For 3000 cycles, the reflectivity plots are shifted by a factor of 10 and the spin ASY by −0.5 for clarity.

Fig. 5. XRR reflectivity of the Ni/NiO$_x$ sample as a function of Q before cycling and after 3,000, 10,000, and 20,000 charging-discharging cycles, with experimental data (symbols) and fits (lines). The plots are shifted by factors of 10 respectively for clarity. Inset: zoom-in of the 10,000 cycles plot at the low Q range.

and XRR data allows to determine fine details of the layer thickness and interface changes of the Ni, NiO$_x$ and the newly-formed layers upon cyclic charging-discharging.

A true co-refinement of PNR and XRR data sets using the exact same set of structural parameters remained out of scope for our investigation, because minor parameter differences (i.e., individual layer thicknesses) in as-prepared sample pieces were expected. However, the analyses of the XRR and PNR data sets (Fig. 6 and Table 1) are very consistent. For all fitted parameters numerically displayed in Table 1, consistently the same numbers are used and fixed when analyzing PNR and XRR SLD profiles for the as-prepared samples and the state of the samples after certain cycling numbers. Theoretical chemical SLD values for the Si substrate are used, as well as for the D$_2$O-based electrolyte as the concentration of NaOH in D$_2$O is extremely low and the deviation can be neglected. The relevant fitting parameters of the Ni/NiO$_x$ sample, such as thickness, atomic density, stoichiometry of the sub-layers, and the magnetic moment within the Ni sub-layer as a function of sample depth, are varied. In regard to the as-prepared sample, the derived density of the Ni layer (6.85 g cm^{-3}) is about 77% of the theoretical value (8.89 g cm^{-3}). The magnetic moments within the Ni layer correspond to 0.60 μ_B per Ni atom, i.e., the same value as bulk Ni at room temperature. The Ni layer is 76.6 nm thick and the NiO$_x$ layer is 25.0 nm thick by PNR fitting results. While the Ni layer is determined to be 77.2 nm thick and the NiO$_x$ is 24.1 nm thick by XRR fitting results. Both PNR and XRR thickness fitting results are in good agreement with our observations using TEM.

The chemical and magnetic SLD profiles obtained by PNR and XRR analyses, before and after cycling the Ni/NiO$_x$ sample through 3000 cycles, are compared, together with the chemical SLD profiles for the nominal Ni(75 nm)/NiO(25 nm) bilayer (Fig. 6). Additional

chemical SLD profiles obtained from extended 10,000 and 20,000 cycling are also shown (XRR analysis only). The fitting parameters which were obtained by independently fitting the PNR and XRR data sets are consistent and within the error bars of the data. According to the PNR SLD profiles, the outer part of the NiO$_x$ layer near the interface to the electrolyte contains a ferromagnetic volume about 5 nm in depth. This indicates a local presence of Ni particles. Another important finding is that the outer ferromagnetic volume basically remains unchanged, while its location and the Ni/NiO$_x$ interface are shifted towards the Ni layer after 3000 cycles. This thickness consumption may be ascribed to two processes occurring in parallel during the lower thousands of cycles: (1) The consumption of oxide within the NiO$_x$ layer. The Ni oxide dissolves during cycling, because of anion intercalation-deintercalation and the resultant breaking of crystal structure [44]. This process reduces the thickness of the NiO$_x$ layer. (2) The consumption of Ni at the Ni/NiO$_x$ interface. The Ni is oxidized into oxide at the Ni/NiO$_x$ interface by the anodic voltage during cycling [38,45,46]. This reduces the thickness of the Ni layer but increases that of the NiO$_x$ layer. The observed *ca.* 2 nm total thickness depletion is a consequence of both effects. Note that, despite the PNR SLD of NiO$_x$ being low at the interface to the Ni layer, it increases steeply towards the outer film surface. XRR results show a systematic evolution that in larger cycle numbers, the top of the NiO$_x$ layer at the interface to the electrolyte shows a first decreased and then increased SLD, while the SLD of NiO$_x$ deeper below at the interface to the Ni layer increases monotonously to higher values than within the Ni layer. Moreover, the total thickness of the sample hardly changes in the XRR measurements. These characteristics of the NiO$_x$ layer represents the variation of the interior structure and composition upon higher thousands of cycles: (1) For the top of the NiO$_x$ layer, as also
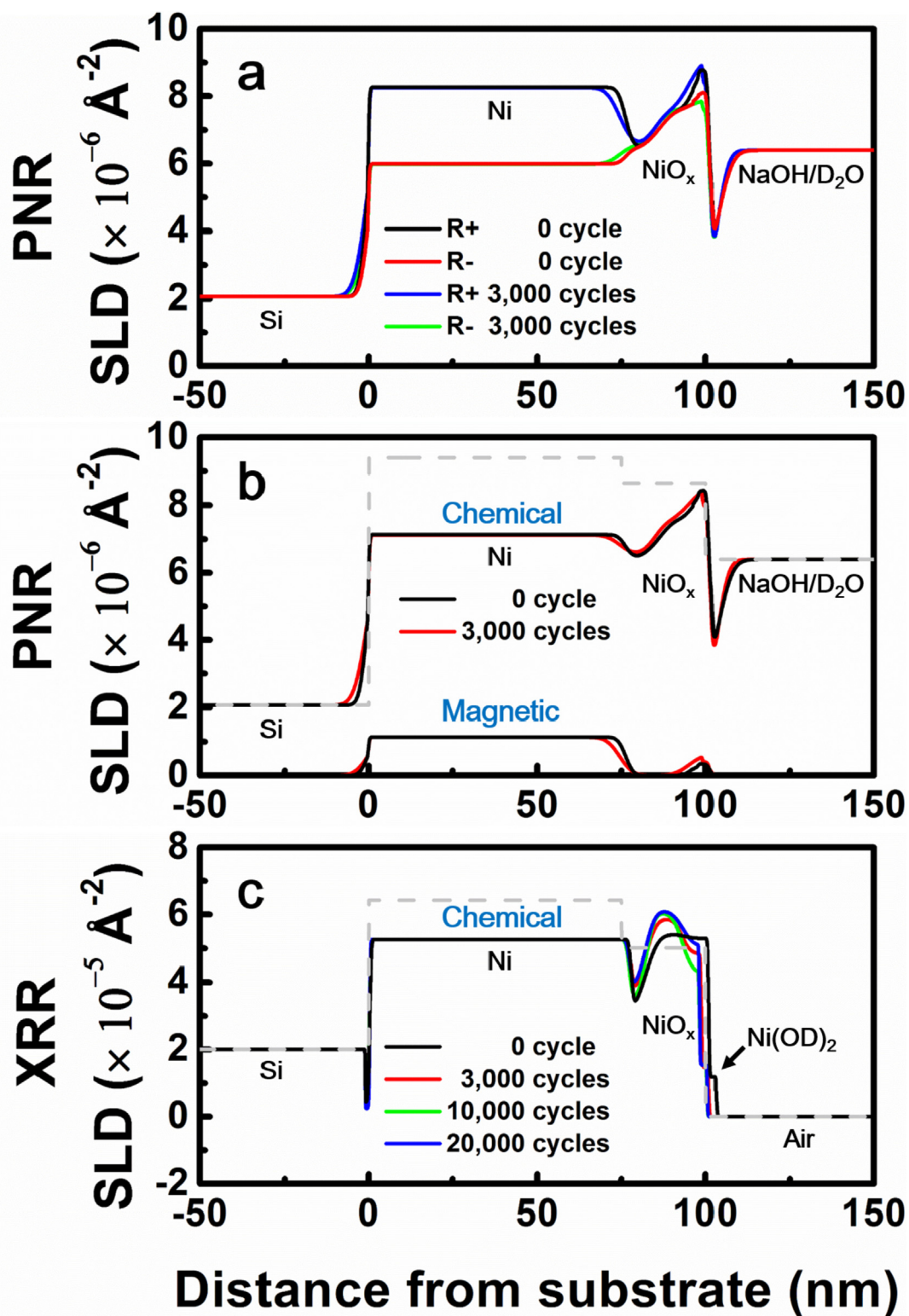
Fig. 6. (a) PNR spin-up (R+) and spin-down (R-) SLD profiles of sample obtained before cycling and after 3000 charging-discharging cycles; (b) PNR chemical/magnetic SLD profiles of the Ni/NiO$_x$ sample obtained before cycling and after 3000 charging-discharging cycles; (c) XRR chemical SLD profiles of sample obtained before cycling and after 3,000, 10,000, and 20,000 charging-discharging cycles. Dashed lines: PNR and XRR chemical SLD profiles of the nominal Ni(75 nm)/NiO(25mn) bilayer.

addressed in the CV results (Fig. 3), the dissolution of NiO within the NiO$_x$ layer (and also the later Ni(OD)$_2$ layer) always exists in the course of cycling. However, from the perspective of high cycle numbers, the dissolution of NiO is via a dominant "hole drilling"

behavior other than "flat grinding", i.e. the "more porous" part dissolves through crystal structure breaking and the "more compact" part is preserved. (2) For the bottom of the NiO$_x$ layer, the increase of derived density reflects the electrochemical redox

Table 1
Theoretical and fitted density and SLD values for materials involved. The fitted spin-up (R+) and spin-down (R-) PNR SLD correspond to $0.60\mu_B$ per Ni atom (identical to bulk Ni at room temperature).

Layer	Density (g cm^{-3})		PNR SLD ($\times 10^{-6}$ Å^{-2})		XRR SLD ($\times 10^{-5}$ Å^{-2})	
	Theoretical	Fitted	Theoretical	Fitted	Theoretical	Fitted
Si	2.33	2.33	2.07	2.07	2.00	2.00
Ni	8.89	6.85	9.40	7.24	6.43	5.26
Ni (R+)	8.89	6.85	10.87	8.37	N/A	N/A
Ni (R-)	8.89	6.85	7.94	6.11	N/A	N/A
NiO	6.67	variable	8.66	variable	5.01	variable
Ni(OD)$_2$	4.10	variable	9.19	variable	3.24	variable
D$_2$O	1.11	1.11	6.39	6.39	N/A	N/A

Fig. 7. Top view SEM images of the Ni/NiO$_x$ sample after 20,000 cycles of charging-discharging at: (a) low magnification (inset: as-prepared sample) and (b) high magnification.

reactions and anion intercalation-deintercalation causes a repair of crystal defects, probably by means of Ni atom rearrangement, filling of oxygen vacancies within NiO$_x$, or both. As already discussed in Figs. 4 and 5, a characteristic low-SLD layer of 2 nm is refined between the NiO$_x$ layer and the electrolyte. Because NiO is readily hydrated by aqueous electrolytes, we believe that this layer volume consists of Ni(OD)$_2$ and the derived density of Ni(OD)$_2$ equals to 47% of its bulk value. The diffuse slope of the SLD into the D$_2$O layer indicates a large surface roughness of the Ni(OD)$_2$. The sensitivity for the Ni(OD)$_2$ layer is weak in the PNR measurements due to the similar SLD values of the porous NiO$_x$ and D$_2$O, the rough outer surface and the limited Q range, while it is much more pronounced through the well-defined characteristic feature appearing at 4.5 nm^{-1} in the XRR measurement (Fig. 5). The Ni(OD)$_2$ layer retains a basically unchanged thickness of 2 nm irrespective of the charging-discharging cycle number, indicating that the 2 nm thick Ni(OD)$_2$ layer we observed is a result of dynamic equilibrium between NiO-to-Ni(OD)$_2$ and Ni(OD)$_2$ dissolution. Since Ni(OD)$_2$ is also involved in the redox reactions and undergoes the anion intercalation-deintercalation, the crystal structure of Ni(OD)$_2$ can also be broken, which leads to the dissolving of Ni(OD)$_2$. However, the thickness of the Ni(OD)$_2$ layer will be almost constant, because the newly exposed NiO underneath the dissolving Ni(OD)$_2$ will be immediately hydrated into Ni(OD)$_2$ in the electrolyte. A notable dip in the XRR SLD is observed at the Si/Ni interface, which exists already before cycling and does not change with increasing cycle numbers. This is likely caused by a residual hydrocarbon layer left-over from the sample preparation process, rather than a SiO$_2$ layer. Despite that the naturally oxidized SiO$_2$ (likely a few monolayers) on the surface of the Si substrate is not removed prior to sample deposition, the presence of such layer is unable to be detected during the XRR measurements. This is because the XRR SLD values of Si and SiO$_2$ are very similar (e.g., the XRR SLD of Si $= 2.00 \times 10^{-5}$ Å^{-2} and SiO$_2 = 2.27 \times 10^{-5}$ Å^{-2}). Also, a distinct SiO$_2$ layer cannot be distinguished from the Si/Ni interface during the PNR measurements because SiO$_2$ has a PNR SLD half-way between the PNR SLDs of Si and the Ni layer (e.g., the PNR SLD of Si $= 2.07 \times 10^{-6}$ Å^{-2} and SiO$_2 = 4.19 \times 10^{-6}$ Å^{-2}, and the PNR SLD of the Ni layer is $= 7.24 \times 10^{-6}$ Å^{-2}), which essentially means this thin SiO$_2$ layer will "blend" into the interfacial SLD region and will not stand out as a prominent feature in the PNR SLD profiles.

Top-view SEM images of the Ni/NiO$_x$ sample before cycling and after the completion of 20,000 charging-discharging cycles shows an eventual porous network structure is obtained at the sample surface (Fig. 7), in contrast to the as-prepared layered structure (Fig. 2 b). The upper NiO$_x$ layer consists of ligament-connected spherical particles ranging in size from 50 to 100 nm (the "more porous" part), supported by a mesh-like film (the "more compact" part), and the deeper planar Ni layer is partially exposed.
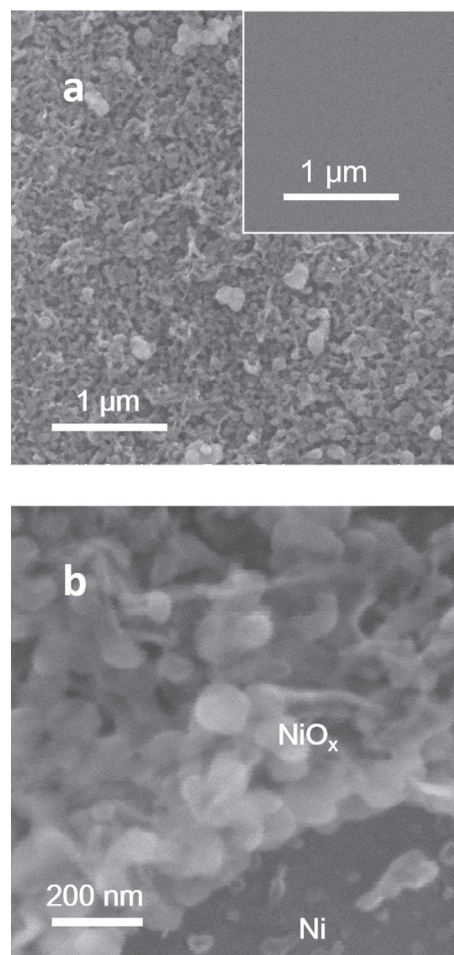
Combining the SEM results with the PNR and XRR analyses, it can be inferred that the structural evolution starts at the NiO$_x$ surface-layer, where nanochannels gradually form within the NiO$_x$ layer via the dissolution of the "more porous" part, leaving the "more compact" part to form a porous network. The transition from a layered to a porous structure increases the specific surface area of the sample, leading to altered CV characteristics and an enhanced capacitance of the Ni/NiO$_x$ supercapacitor after extensive cyclic charging-discharging processes.

4. Conclusion

In summary, using a combination of PNR, XRR, CV, and TEM/SEM, we studied the structural evolution and compositional changes of a layered Ni/NiO$_x$ supercapacitor during cyclic charging-discharging experiments in an alkaline electrolyte for up to 20,000 cycles. The results provide an experimental support that both the current-collecting framework (Ni) and the electroactive material (NiO) of the Ni/NiO$_x$ supercapacitor are consumed in the process of charging-discharging: (1) In the lower thousands of cycles, electrochemical oxidation of the inner Ni and dissolution of the outer Ni oxide contribute to an overall thickness depletion of 2 nm. (2) Upon higher thousands of cycles, the "more porous" part of the NiO$_x$ layer at the sample surface dissolves to form nanochannels, while the "more compact" part is unaffected, and this "hole drilling"

depletion behavior of Ni oxide results in a structural evolution of the film from a layered two-dimensional, into a porous three-dimensional structure. The additional surface area of the Ni/NiO$_x$ supercapacitor generated after charging-discharging cycles gives rise to its increased capacitance. (3) Again in the higher cycle numbers, the crystal defects of inner NiO$_x$ layer are probably eliminated gradually by, for example, Ni atom rearrangement, filling of oxygen vacancies within NiO$_x$, or both.

Acknowledgement

References

[1] I.S. Lee, N. Lee, J. Park, B.H. Kim, Y.W. Yi, T. Kim, T.K. Kim, I.H. Lee, S.R. Paik, T. Hyeon, Ni/NiO core/shell nanoparticles for selective binding and magnetic separation of histidine-tagged proteins, J. Am. Chem. Soc. 128 (2006) 10658—10659.

[2] X. Niu, M. Lan, H. Zhao, C. Chen, Highly sensitive and selective nonenzymatic detection of glucose using three-dimensional porous nickel nanostructures, Anal. Chem. 85 (2013) 3561—3569.

[3] L. He, Z.M. Liao, H.C. Wu, X.X. Tian, D.-S. Xu, G.L.W. Cross, G.S. Duesberg, I.V. Shvets, D.P. Yu, Memory and threshold resistance switching in Ni/NiO core—shell nanowires, Nano Lett. 11 (2011) 4601—4606.

[4] Q. Lu, M.W. Lattanzi, Y. Chen, X. Kou, W. Li, X. Fan, K.M. Unruh, J.G. Chen, J.Q. Xiao, Supercapacitor electrodes with high-energy and power densities prepared from monolithic NiO/Ni nanocomposites, Angew. Chem. 123 (2011) 6979—6982.

[5] W. Wen, J.M. Wu, M.H. Cao, NiO/Ni powders with effective architectures as anode materials in Li-ion batteries, J. Mater. Chem. A 1 (2013) 3881—3885.

[6] C. Parada, E. Morán, Microwave-assisted synthesis and magnetic study of nanosized Ni/NiO materials, Chem. Mater. 18 (2006) 2719—2725.

[7] Y.H. Park, Y.H. Shin, S.J. Noh, Y. Kim, S.S. Lee, C.G. Kim, K.S. An, C.Y. Park, Optical quenching of NiO/Ni coated ZnO nanowires, Appl. Phys. Lett. 91 (2007), 012102.

[8] X. Sun, W. Si, X. Liu, J. Deng, L. Xi, L. Liu, C. Yan, O.G. Schmidt, Multifunctional Ni/NiO hybrid nanomembranes as anode materials for high-rate Li-ion batteries, Nano Energy 9 (2014) 168—175.

[9] J.H. Kim, S.H. Kang, K. Zhu, J.Y. Kim, N.R. Neale, A.J. Frank, Ni-NiO core-shell inverse opal electrodes for supercapacitors, Chem. Commun. 47 (2011) 5214—5216.

[10] G. Wang, L. Zhang, J. Zhang, A review of electrode materials for electrochemical supercapacitors, Chem. Soc. Rev. 41 (2012) 797—828.

[11] J. Joseph, R. Rajagopalan, S.S. Anoop, V. Amruthalakshmi, A. Ajay, S.V. Nair, A. Balakrishnan, Shape tailored Ni$_3$(NO$_3$)$_2$(OH)$_4$ nano-flakes simulating 3-D bouquet-like structures for supercapacitors: exploring the effect of electrolytes on stability and performance, RSC Adv. 4 (2014) 39378—39385.

[12] C. Zhong, Y. Deng, W. Hu, J. Qiao, L. Zhang, J. Zhang, A review of electrolyte materials and compositions for electrochemical supercapacitors, Chem. Soc. Rev. 44 (2015) 7484—7539.

[13] Y.Q. Zhang, X.H. Xia, J.P. Tu, Y.J. Mai, S.J. Shi, X.L. Wang, C.D. Gu, Self-assembled synthesis of hierarchically porous NiO film and its application for electrochemical capacitors, J. Power Sources 199 (2012) 413—417.

[14] M. Hasan, M. Jamal, K.M. Razeeb, Coaxial NiO/Ni nanowire arrays for high performance pseudocapacitor applications, Electrochim. Acta 60 (2012) 193—200.

[15] C. Yuan, X. Zhang, L. Su, B. Gao, L. Shen, Facile synthesis and self-assembly of hierarchical porous NiO nano/micro spherical superstructures for high performance supercapacitors, J. Mater. Chem. 19 (2009) 5772—5777.

[16] X. Zhang, W. Shi, J. Zhu, W. Zhao, J. Ma, S. Mhaisalkar, T.L. Maria, Y. Yang, H. Zhang, H.H. Hng, Synthesis of porous NiO nanocrystals with controllable surface area and their application as supercapacitor electrodes, Nano Res. 3 (2010) 643—652.

[17] W. Xing, S. Qiao, X. Wu, X. Gao, J. Zhou, S. Zhuo, S.B. Hartono, D. Hulicova-Jurcakova, Exaggerated capacitance using electrochemically active nickel foam as current collector in electrochemical measurement, J. Power Sources 196 (2011) 4123—4127.

[18] M. Liu, J. Chang, J. Sun, L. Gao, A facile preparation of NiO/Ni composites as high-performance pseudocapacitor materials, RSC Adv. 3 (2013) 8003—8008.

[19] S. Langridge, J. Schmalian, C.H. Marrows, D.T. Dekadjevi, B.J. Hickey, Quantification of magnetic domain disorder and correlations in antiferromagnetically coupled multilayers by neutron reflectometry, Phys. Rev. Lett. 85 (2000) 4964.

[20] H. Hillborg, J.F. Ankner, U.W. Gedde, G.D. Smith, H.K. Yasuda, K. Wikström, Crosslinked polydimethylsiloxane exposed to oxygen plasma studied by neutron reflectometry and other surface specific techniques, Polymer 41 (2000) 6851—6863.

[21] J.A. Dura, D.J. Pierce, C.F. Majkrzak, N.C. Maliszewskyj, D.J. McGillivray, M. Lösche, K.V. O'Donovan, M. Mihailescu, U. Perez-Salas, D.L. Worcester, AND/R: advanced neutron diffractometer/reflectometer for investigation of thin films and multilayers for the life sciences, Rev. Sci. Instrum. 77 (2006), 074301.

[22] B.P. Toperverg, Polarized neutron reflectometry of magnetic nanostructures, Phys. Met. Metallogr. 116 (2015) 1337—1375.

[23] M.R. Fitzsimmons, I.K. Schuller, Neutron scattering—the key characterization tool for nanostructured magnetic materials, J. Magn. Magn. Mater. 350 (2014) 199—208.

[24] H. Zabel, K. Theis-Brohl, M. Wolff, B.P. Toperverg, Polarized neutron reflectometry for the analysis of nanomagnetic systems, IEEE Trans. Magn. 44 (2008) 1928—1934.

[25] C.F. Majkrzak, Polarized neutron reflectometry, Phys. B Condens. Matter 173 (1991) 75—88.

[26] J.F. Ankner, G.P. Felcher, Polarized-neutron reflectometry, J. Magn. Magn. Mater. 200 (1999) 741—754.

[27] J. Daillant, A. Gibaud, X-ray and Neutron Reflectivity: Principles and Applications, Springer, 2008.

[28] X.L. Zhou, S.H. Chen, Theoretical foundation of X-ray and neutron reflectometry, Phys. Rep. 257 (1995) 223—348.

[29] T.P. Russell, X-ray and neutron reflectivity for the investigation of polymers, Mater. Sci. Rep. 5 (1990) 171—271.

[30] P.M. Saville, M. Gonsalves, A.R. Hillman, R. Cubitt, Dynamic neutron reflectivity measurements during redox switching of nickel hydroxide films, J. Phys. Chem. B 101 (1997) 1—4.

[31] A. Glidle, A.R. Hillman, K.S. Ryder, E.L. Smith, J. Cooper, N. Gadegaard, J.R.P. Webster, R. Dalgliesh, R. Cubitt, Use of neutron reflectivity to measure the dynamics of solvation and structural changes in polyvinylferrocene films during electrochemically controlled redox cycling, Langmuir 25 (2008) 4093—4103.

[32] J.E. Owejan, J.P. Owejan, S.C. DeCaluwe, J.A. Dura, Solid electrolyte interphase in Li-ion batteries: evolving structures measured in situ by neutron reflectometry, Chem. Mater. 24 (2012) 2133—2140.

[33] T.M. Fears, M. Doucet, J.F. Browning, J.K.S. Baldwin, J.G. Winiarz, H. Kaiser, H. Taub, R.L. Sacci, G.M. Veith, Evaluating the solid electrolyte interphase formed on silicon electrodes: a comparison of ex situ X-ray photoelectron spectroscopy and in situ neutron reflectometry, Phys. Chem. Chem. Phys. 18 (2016) 13927—13940.

[34] B. Jerliu, L. Dörrer, E. Hüger, G. Borchardt, R. Steitz, U. Geckle, V. Oberst, M. Bruns, O. Schneider, H. Schmidt, Neutron reflectometry studies on the lithiation of amorphous silicon electrodes in lithium-ion batteries, Phys. Chem. Chem. Phys. 15 (2013) 7777—7784.

[35] B. Jerliu, E. Hüger, L. Dorrer, B.K. Seidlhofer, R. Steitz, V. Oberst, U. Geckle, M. Bruns, H. Schmidt, Volume expansion during lithiation of amorphous silicon thin film electrodes studied by in-operando neutron reflectometry, J. Phys. Chem. C 118 (2014) 9395—9399.

[36] E. Hüger, J. Stahn, H. Schmidt, Neutron reflectometry to measure in situ Li permeation through ultrathin silicon layers and interfaces, J. Electrochem. Soc. 162 (2015) A7104—A7109.

[37] F. Strauß, E. Hüger, P. Heitjans, T. Geue, J. Stahn, H. Schmidt, Lithium permeation through thin lithium—silicon films for battery applications investigated by neutron reflectometry, Energy Technol. 4 (2016) 1582—1587.

[38] M. Vezvaie, P. Kalisvaart, H. Fritzsche, Z. Tun, D. Mitlin, The penetration depth of chemical reactions in a thin-film Co$_3$O$_4$ supercapacitor electrode, J. Electrochem. Soc. 161 (2014) A798—A802.

[39] J.Y. Guo, J. van Lierop, S.Y. Chang, K.W. Lin, Magnetic and magnetotransport properties of exchange-biased NiFe/NiO bilayers, Jpn. J. Appl. Phys. 48 (2009) 073004.

[40] M. James, A. Nelson, S.A. Holt, T. Saerbeck, W.A. Hamilton, F. Klose, The multipurpose time-of-flight neutron reflectometer "Platypus" at Australia's OPAL reactor, Nucl. Instrum. Meth. Phys. Res. A 632 (2011) 112—123.

[41] T. Saerbeck, F. Klose, A.P. Le Brun, J. Fuzi, A. Brule, A. Nelson, S.A. Holt, M. James, Polarization "Down under": the polarized time of flight neutronreflectometer PLATYPUS, Rev. Sci. Instrum. 83 (2012), 081301.

[42] SimulReflec, Lab, Leon Brillouin, CEA/CNRS UMR12, France, 2007. Free software available, http://www.llb.cea.fr/prism/programs/simulreflec/simulreflec.html.

[43] J. Cheng, G.P. Gao, S.Y. Yang, Characterization of sol-gel-derived NiO$_x$ xerogels as supercapacitors, J. Power Sources 159 (2006) 734—741.

[44] Y. Liu, N. Fu, G. Zhang, W. Lu, L. Zhou, H. Huang, Ni@NiO core/shell dendrites for ultra-long cycle life electrochemical energy storage, J. Mater. Chem. A 4 (2016) 15049—15056.

[45] C.A. Lucas, A. Kowal, R.J. Nichols, D. Johnson, S.L. Medway, In situ studies of the oxidation of nickel electrodes in alkaline solution, J. Electroanal. Chem. 587 (2006) 172–181.

[46] X. Dai, D. Chen, H. Fan, Y. Zhong, L. Chang, H. Shao, J. Wang, J. Zhang, C.N. Cao, $Ni(OH)_2$/NiO/Ni composite nanotube arrays for high-performance super-capacitors, Electrochim. Acta 154 (2015) 128–135.